Supplementary Information

Manipulating Atomic Defects in Plasmonic Vanadium Dioxide for Superior Solar and Thermal Management

Yujie Ke [1], Bikun Zhang [2], Tao Wang [3], Yaxu Zhong [4], Tuan Duc Vu [1,5], Shancheng Wang [1], Yang Liu [4], Shlomo Magdassi [6,7], Xingchen Ye [4], Dongyuan Zhao,[8] Qihua Xiong,[9] Zhimei Sun [2,*], Yi Long [1,7,10,*].

1. School of Materials Science and Engineering, Nanyang Technological University, Singapore, 639798, Singapore.
2. School of Materials Science and Engineering & Centre for Integrated Computational Materials Science, International Research Institute for Multidisciplinary Science, Beihang University, Beijing, 100191, China.
3. Institute of Functional Nano & Soft Materials (FUNSOM), Jiangsu Key Laboratory for Carbon-Based Functional Materials & Devices, Collaborative Innovation Center of Suzhou Nano Science and Technology, Soochow University, Suzhou, Jiangsu, 215123, China.
4. Department of Chemistry, Indiana University Bloomington, Bloomington, Indiana, 47405, United States.
5. Singapore Institute of Manufacturing Technology (SIMTech), Innovis, Singapore, 138634, Singapore.
6. Casali Center of Applied Chemistry, Institute of Chemistry, The Hebrew University of Jerusalem, Jerusalem, 91904, Israel.
7. Singapore-HUJ Alliance for Research and Enterprise (SHARE), Campus for Research Excellence and Technological Enterprise (CREATE), Singapore, 138602, Singapore.
8. Department of Chemistry, Shanghai Key Laboratory of Molecular Catalysis and Innovative Materials, Laboratory of Advanced Materials, iChEM (Collaborative Innovation Center of Chemistry for Energy Materials), Fudan University, Shanghai, 200433, China.
9. Division of Physics and Applied Physics, School of Physical and Mathematical Sciences, Nanyang Technological University, Singapore, 637371, Singapore.
10. Sino-Singapore International Joint Research Institute (SSIJRI), Guangzhou, 510000, China.

* Corresponding author:
Zhimei Sun (zmsun@buaa.edu.cn), Yi Long (longyi@ntu.edu.sg)

Content

Methods

Preparation of vanadium precursors. The sol-gel method was applied for the precursor preparation.[1, 2] The Mg (99.9%, Alfa Aesar) and W (99.9%, Alfa Aesar) powders were dissolved in 15 ml hydrogen peroxide (H_2O_2, 30%, Sigma-Aldrich) at 90 ^oC by 5-h stirring. The dopant weight is calculated according to the targeting doping levels in atm.%. After that, 180 mg of vanadium pentoxide (V_2O_5, 99.6%, Alfa Aesar) powder and 400 mg of oxalic acid (99.99%, Alfa Aesar) are added, following by a mixing process of 2 h at 90 ^oC. Be very careful with the violent reaction of H_2O_2 and V_2O_5.

Preparation of colloidal templates. A water-air interfacial assembly method is applied.[1, 3] In detail, the pre-dispersed polystyrene sphere solution was dropped slowly onto a glass slide surrounded by water. The pre-dispersed solution contains 0.2 wt.% of polystyrene spheres (200 nm, 10%, Sigma-Aldrich) in a water/ethanol (1:1 in volume) mixture. The nanospheres on the glass slide spread out spontaneously and gradually self-assembled on the water-air interface. The monolayer was consolidated by adding several droplets of the 0.2 wt.% sodium dodecyl sulfate (SDS, 99%, Sigma-Aldrich) solution. The monolayer template was picked up by quartz substrates and dried in 100 ^oC for 2 h. After that, an O-plasma treatment (300W, 10s) is applied to make templates hydrophilic.

Preparation of NP arrays. A vertically dip-coating method is applied to coat the vanadium precursor solution onto colloidal templates. The dip-coated speed is 120 mm/min. Coated samples are dried in the air, followed by an annealing process at 600 ^oC for 2h for the so-called pristine VO_2. Argon gas was applied with a continuous flow speed of 200 ml/min. The multilayer sample is achieved by simply stacking each doped/co-doped VO_2 NPs layer with quartz substrates.

Atomic defects control. The substitutional doping level in produced NPs is modulated by controlling the dopant concentration in precursors before annealing processes. The degrees of O vacancies are controlled by changing the annealing temperatures between 500 and 750 ^{o}C while maintaining the annealing durations and atmosphere. The surface oxidization degrees are controlled by varying the duration (1 – 54 mins) of the post-treatment O-plasma for produced samples.

Characterizations. The crystal structure was characterized using a thin-film X-ray diffraction (XRD, Shimadzu XRD-6000) at room temperature with a fixed incident angle 1.0 ^{o}. Transmission electron microscopy (TEM, Carl Zeiss, LIBRA@120) was performed at an accelerating voltage of 200 kV. TEM sample is prepared by scraping from substrates with the assistance of ethanol. Transmittance spectra were recorded by using a UV-vis-NIR spectrophotometry (Cary 5000, Agilent Ltd.) with a digital-controlled heating-cooling accessory (Linkam PE120). The nano\microscale morphology measurement was conducted by using the field-emission scanning electron microscope (SEM, JEOL, 7600F). Elemental valances are analyzed using X-ray photoelectron spectra (XPS, Thermo ESCALab 250i-XL & Thetaprobe A1333). Elemental ratios are measured using the energy-dispersive X-ray spectroscopy on an SEM (SEM, JEOL, 7600F) and further confirmed using a TEM (TEM, JEOL, 2100F). The crystal topography and height are identified by using atomic force microscopy (AFM, Bruker, DI-3100). Analysis of surface composition is conducted using a Raman spectrum (Renishaw inVia Raman microscope) with a 10% powered 514 nm laser. The same heating accessory (Linkam PE120) assists in high-temperature Rama spectrum measurement.

DFT simulation. The DFT calculations were performed using the Vienna Ab initio Simulation Package (VASP). The generalized gradient approximation (GGA) with Perdew−Burke−Ernzerhof (PBE) exchange-correlation potential was employed. Considering

the partially-filled d-orbitals of V and W atoms, DFT+U was applied with the effective on-site Coulomb/Exchange interaction parameters being 4.2/0.8 eV and 3.0/0.0 eV for V and W atoms respectively according to the previous work. The cut-off energy was set to 520 eV. 2×2×2 supercells with 16 metal atoms and 32 O atoms were applied and the ratio of doping atoms to V atoms was 1 to 15, thus a doping level of 6.25 at. %. Besides, 2×2×3 supercells with vacuum layers of 20 Å were used to study the effect of surface oxidization. The bulk structures were fully relaxed while for the surface structures only the two outer atomic layers were relaxed under the convergence criteria of |0.01| eV/ Å using the Gaussian smearing method with 0.2 eV of broadening width. For the electronic structure calculations, the energy convergence criteria were set to 10^{-6} eV/atom using the tetrahedron method with Blöchl corrections. During the structure optimization, 5×5×8 and 5×5×6 Monkhorst−Pack k-grids were used while 7×7×12 and 7×7×18 k-grids were used in electronic structure calculations for 2×2×2 and 2×2×3 supercells, respectively.

FDTD simulation. The transmission spectra were calculated by the 3D-FDTD method using Lumerical FDTD Solutions V8.5. In the simulation, the light source was a plane wave; the incident angle was normal to the sample surface; the boundary conditions were periodic. A fine mesh size of 1 nm × 1 nm × 0.5 nm was used. The transmittance spectra were recorded 1000 nm below the sample surface. The optical dielectric constant of VO_2 was adopted from previous reports.[4]

Drude fitting. The Drude fitting of extinction (*E*) spectra were performed using a customized Matlab Script.[5] The *E* spectra of patterned NCs on quartz substrates are described by the Beer−Lambert law:

$$E = \frac{N\sigma_A l}{\ln(10)} \quad (1)$$

where N and l is the filling factor and path length of the patterned NCs. According to Mie theory, the extinction cross-section (σ_A) of spherical NCs are calculated by:

$$\sigma_A = 4\pi k r^3 Imag\left(\frac{\varepsilon_{(\omega)} - \varepsilon_m}{\varepsilon_{(\omega)} + 2\varepsilon_m}\right) \quad (2)$$

where r and $\varepsilon_{(\omega)}$ is the radius and dielectric function of NCs, respectively. The ε_m is the dielectric constant of the surrounding medium, the air. The k is the wave vector of the incident light and is expressed as:

$$k = \sqrt{\varepsilon_m}\frac{\omega}{c} \quad (3)$$

The frequency-dependent dielectric function is calculated by:

$$\varepsilon_{(\omega)} = \varepsilon_\infty - \frac{\omega_p^2}{(\omega^2 + i\omega\Gamma)} \quad (4)$$

where ε_∞ is the dielectric constant at high frequency and ε_∞ = 3.5 of metallic VO_2. ω_p is the bulk plasma frequency and Γ is the free carrier damping constant. The two values of ω_p and Γ are retrieved via the Drude fitting of extinction spectra and summarized in Table S1-4. The N_e, free carrier density, is given by:

$$\omega_P = \sqrt{\frac{N_e e^2}{m^* \varepsilon_0}} \quad (5)$$

where e is the elementary charge, ε_0 is the vacuum permittivity, and m* is the effective mass of electrons, which is 3.5 m^0 for metallic VO_2 according to literature.[6]

Analysis of LSPR intensity and NIR/visible transmittance. The $T_{NIR/vib}$ are based on the integrated transmittance in specific ranges: visible from 380 to 780 nm and NIR from 780 to 2500 nm. The normalized LSPR intensity at a certain temperature (τ) is calculated as：

$$Normalized\ LSPR\ intensity = \frac{\int_{500}^{2500} T(\lambda)_{\tau} d\lambda - \int_{500}^{2500} T(\lambda)_{20^oC} d\lambda}{\int_{500}^{2500} T(\lambda)_{100^oC} d\lambda - \int_{500}^{2500} T(\lambda)_{20^oC} d\lambda} \quad (6)$$

where $T(\lambda)$ is the transmittance at a certain wavelength of λ.

Evaluation for SERS application. SERS were performed using a confocal Raman system (WITEC alpha 300R) with a 532 nm excitation laser and 600 lines/mm grating. The analyte of crystal violet (Sigma-Aldrich) was diluted in DI water with a concentration of 1 x 10^{-5} and was drop-casted onto O-deficient VO_2 substrates produced under 650 ^oC annealing. A digital-controlled heating-cooling accessory (Linkam PE120) is applied for temperature-dependent Raman measurement.

Preparation of IR encryption inks. The ink is prepared by dissolving the defective VO_2 NPs in ethanol (95%, Sigma-Aldrich). In general, the produced defective NPs on substrates (>100 pieces) is peeled off using a doctor blade method, following by dissolving into ~2 ml ethanol. A ~2-h ultrasonic and a~10 mins vortex process is applied to facilitate the NP dispersion for ink application.

Fabrication of the flexible thermal camouflage films. The pristine, O-deficient, and W-doped VO_2 NPs are pealed off from the substrates and re-dissolved into ethanol. Then, the solutions are coated onto the 3M VHB tape using the doctor blade method with a mask of three hollow squares. The coated tape is tried under room temperature, following by the mask removal.

Performance assessment for energy-efficient windows. The performance analysis method is the same as it in the literature.[7] $\Delta T_{lum/sol/NIR}$ is the difference between $T_{lum/sol/sol\text{-}NIR}$ measured at 20 and 100 ^oC. The integral luminous transmittance, T_{lum}, T_{sol}, and $T_{sol\text{-}NIR}$ are calculated as:

$$T_{lum} = \frac{\int_{380}^{780} \varphi_{lum}(\lambda)\, T(\lambda) d\lambda}{\int_{380}^{780} \varphi_{lum}(\lambda) d\lambda} \tag{7}$$

$$T_{sol/sol-NIR} = \frac{\int_{250}^{2500} \varphi_{sol/sol-NIR}(\lambda)\, T(\lambda) d\lambda}{\int_{250}^{2500} \varphi_{sol/sol-NIR}(\lambda) d\lambda} \tag{8}$$

where $\varphi_{\mathrm{lum}}(\lambda)$ is the standard luminous efficiency function of photopic vision in the wavelength range of 380–780 nm, and $\varphi_{\mathrm{sol/NIR}}(\lambda)$ is the solar irradiance spectrum for air mass 1.5 (corresponding to the sun standing 37° above the horizon with 1.5-atmosphere thickness).

Supplementary Fig. 1-10

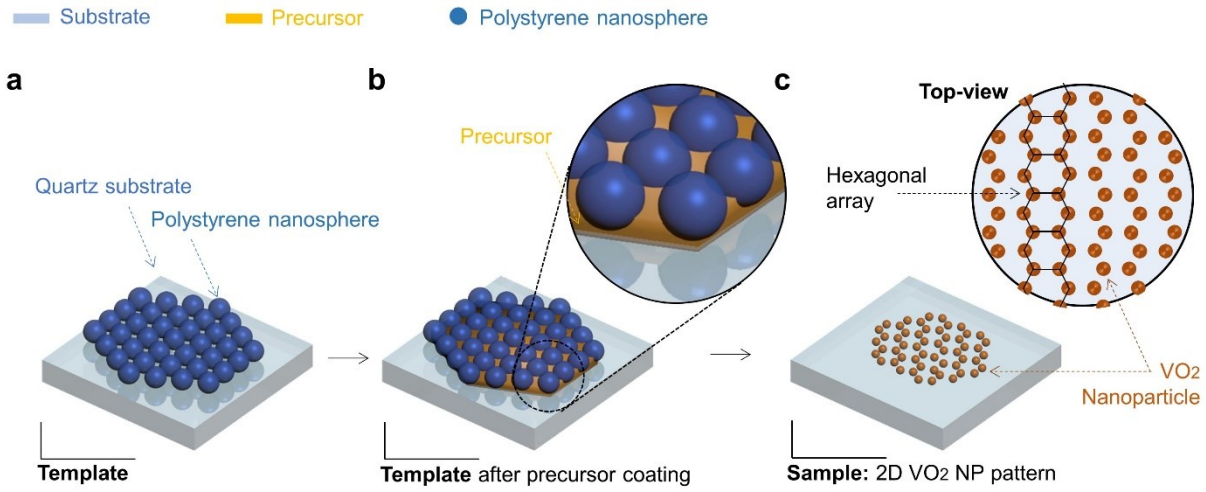

Fig. S1. Schematics of the colloidal lithography method for patterned VO_2. a) The colloidal templates on a quartz substrate consisted of monolayered close-packed polystyrene nanospheres. b) The template with infiltrated vanadium precursor through a dip-coating process. The coated precursor lay on the gaps among nanospheres. c) The produced hexagonal VO_2 nanoparticle arrays after a high-temperature annealing process. During the annealing process, the organic template is removed, and the precursor is crystallized to form VO_2(M/R). An NP forms from the precursor located in the gap among three adjacent nanospheres, resulting in the hexagonal array structures.

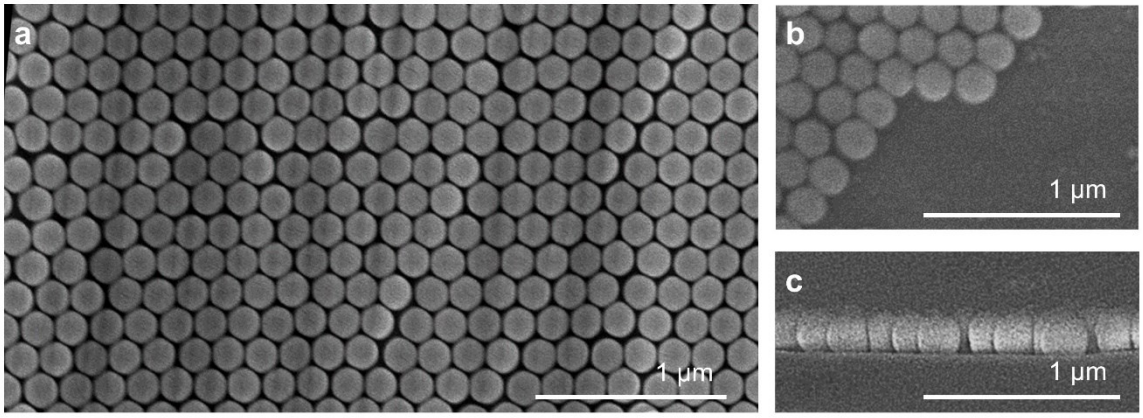

Fig. S2. Monolayer colloidal templates. a) SEM image of the produced colloidal template. b) SEM image of the template on its edge. c) A cross-section view of the template. The template is demonstrated to consist of hexagonal closed-packed nanospheres. The nanospheres display a uniform diameter of ~200 nm. The template is proven to be a monolayer as indicated by the SEM view on its edge and the cross-section view.

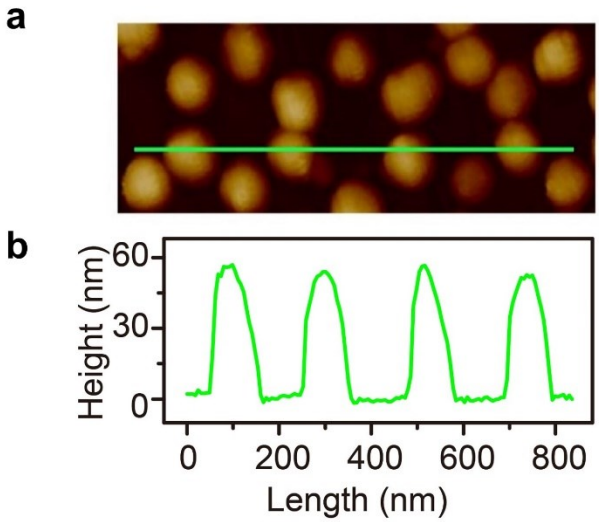

Fig. S3 AFM analysis of VO_2 NPs. a) AFM measurement of the NPs. b) Height analysis of the NPs. The analysis section is indicated as the green line in the Fig. above, covering four NPs, thus four corresponding peaks in height analysis. The NP height is uniform and measured to be ~55 nm.

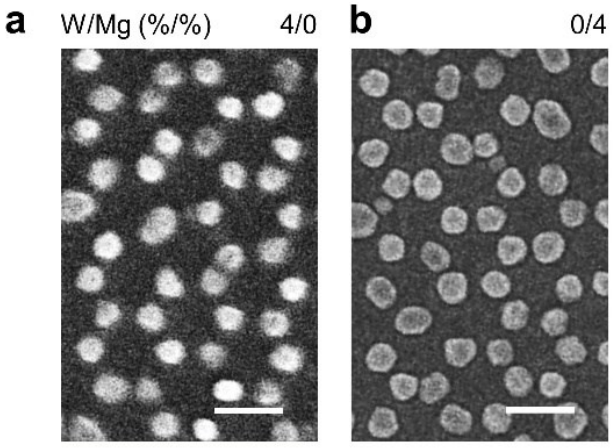

Fig. S4. Supplementary SEM images for single doped samples. a, b) SEM images of representative samples with W/Mg (%/%) doping levels of a) 4/0 and b) 0/4. All samples consist of hexagonal non-closed-packed NP arrays. Though defects exist, no obvious trend is observed under a series doping or co-doping level. The scale bars are 200 nm for the four images.

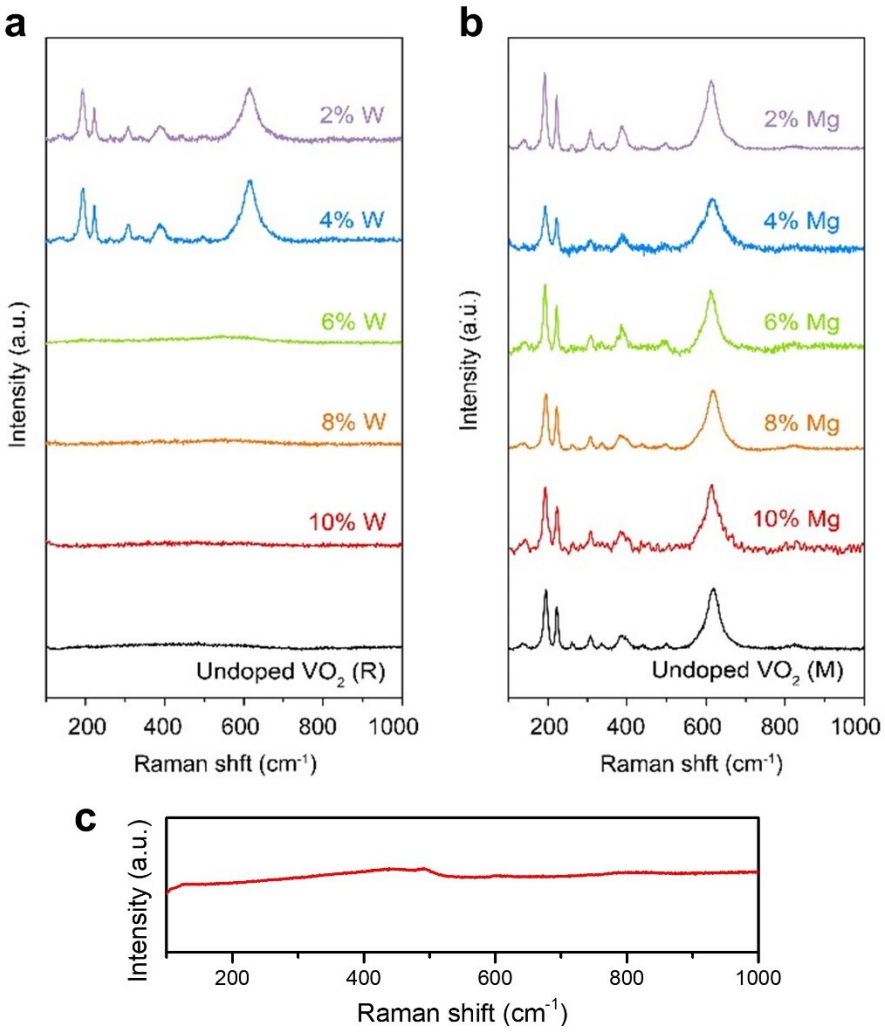

Fig. S5. a, b) Room-temperature Raman spectra of VO_2 NPs with individual a) W or b) Mg dopants. The Raman spectra of undoped VO_2 (R) at high temperature and VO_2 (M) at room-temperature are indicated as black for reference. c) Raman spectrum of a quartz substrate. The measurement is conducted on clean quartz under room temperature. The spectrum is used as a background for the NPs samples.

The characteristic peaks of VO_2 (M) at 190, 220, 390, and 610 cm^{-1} are observed on mildly W-doped (2% - 4%) and all Mg-doped samples, while no identifiable peaks for heavily W-doped samples (6% - 10%) are observed on VO_2 (R) measured at 95 ^oC. The room-temperature R phase in 6-10% W-doped samples is because the introduction of W dopants can lower the transition temperature (τ_c) and stabilize the R phase at room temperature under such doping level, as elaborated in the following paragraph. Similar Raman spectra are also detected on co-doped samples. The results suggest that the VO_2 (M/R) crystal structure is maintained, and there is no emergence of other detectable impurities under W/Mg doping in such doping level (≤10%). Raman spectra were analyzed by removing the substrate quartz background (Fig. S4 c).

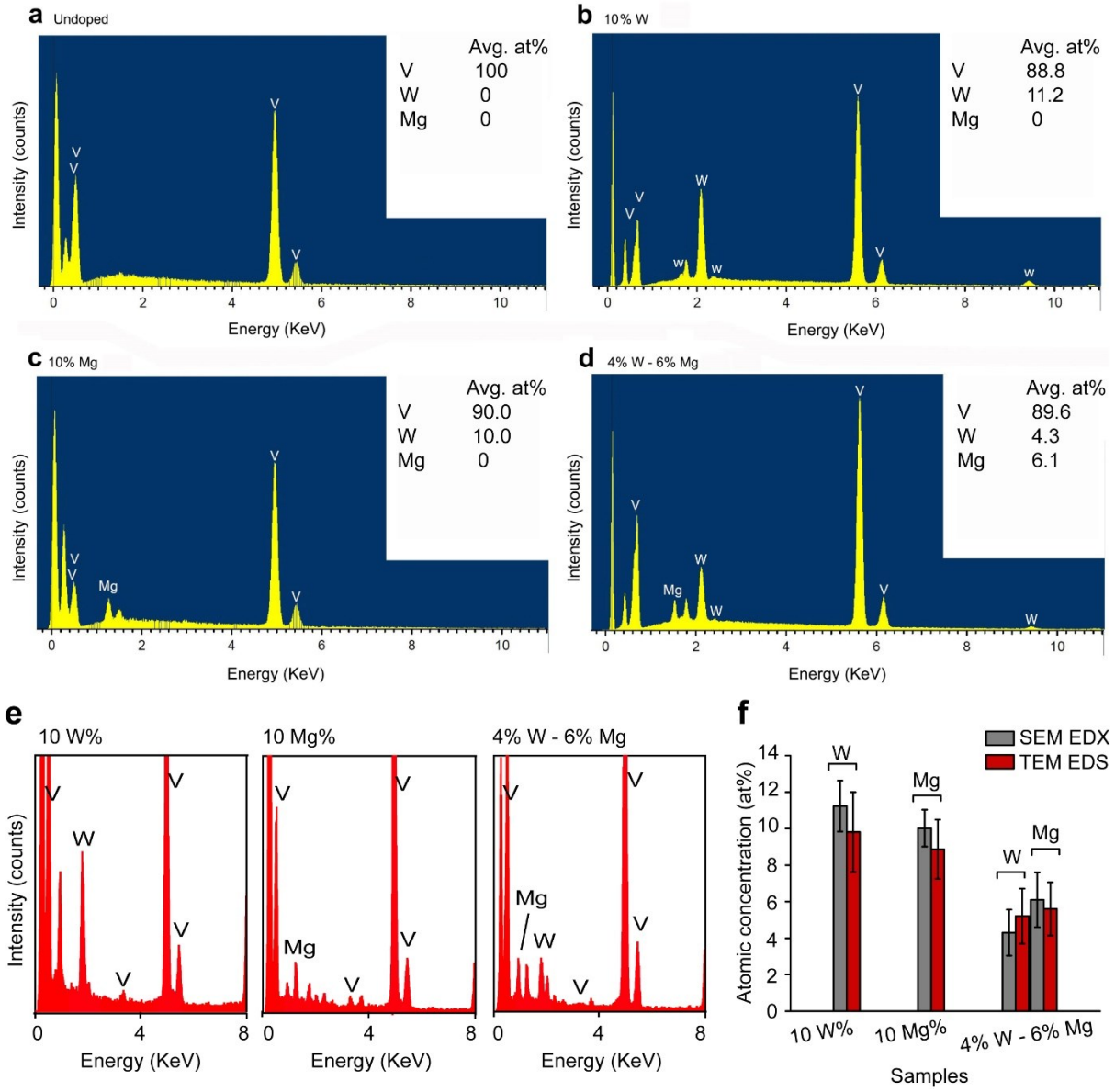

Fig. S6. Representative results of elemental ratio analysis. a-d) The elemental analysis using SEM EDX is presented for four representative samples: a) the undoped, b) the 10% W doped, c) the 10% Mg-doped, and d) 4% W – 6% Mg co-doped samples. e) Elemental analysis using TEM EDX for the 10% W, 10% Mg, and 4% W - 6% Mg samples, respectively. In these analyses, only the elements of V, W, and Mg are considered, and the atomic ratios (AR) are calculated by $AR_{X(X = V, W, \text{ or } Mg)} / AR_V + AR_W + AR_{Mg}$. f) Comparison of the elemental analysis using the SEM and the TEM for the three samples. The doping level identified in samples is closed to the atomic ratio in precursors, and the TEM EDS result is consistent with SEM EDX results, demonstrating the success of the doping level controls in experiments.

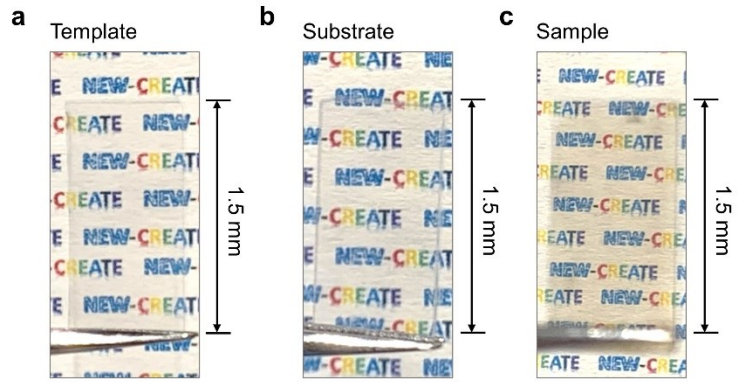

Fig. S7. Photographs of produced samples. Photographs of A) the colloidal template on quartz, B) the pure quartz substrate, and C) a co-doped VO_2 NPs on a quartz substrate. The colloidal template consisted of a 200-nm polystyrene sphere that is highly transparent. The produced samples show a yellow-brown colour compared to the template and the quartz substrate. All samples are transparent, leading to a clear view of the background. The colloidal lithography method here can produce samples in a centimetre-scale.

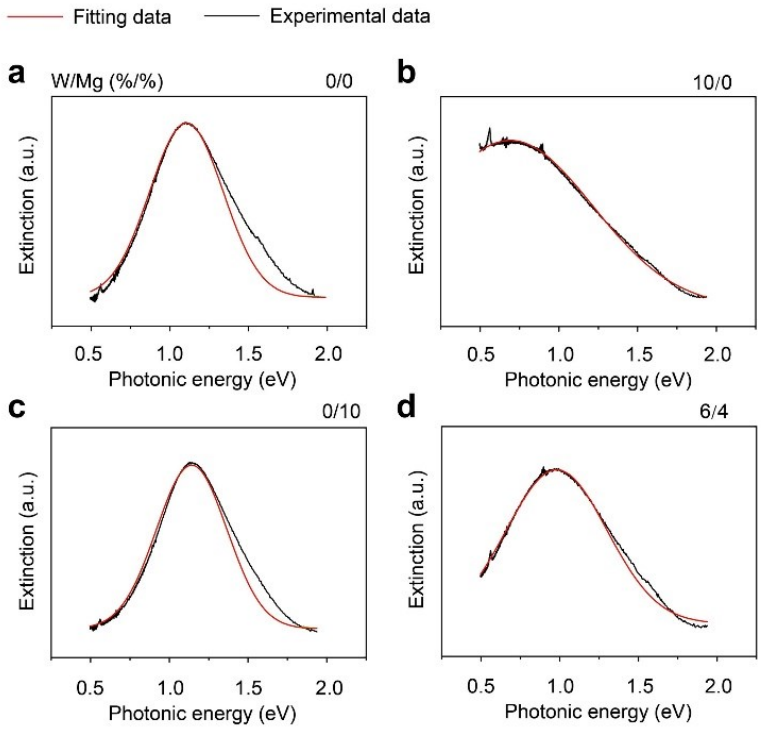

Fig. S8. Gaussian peaking fitting of doped/co-doped samples. The LSPR FWHM is obtained by Gaussian fitting of the extinction peaks. The detailed Gaussian fitting results show as on the four representative samples with different W/Mg (%/%) doping levels: A) 0/0, b) 10/0, c) 0/10, and d) 6/4. The fitting and experimental data are indicated as the red and black lines, respectively. The two data are well-matched with each other on four samples.

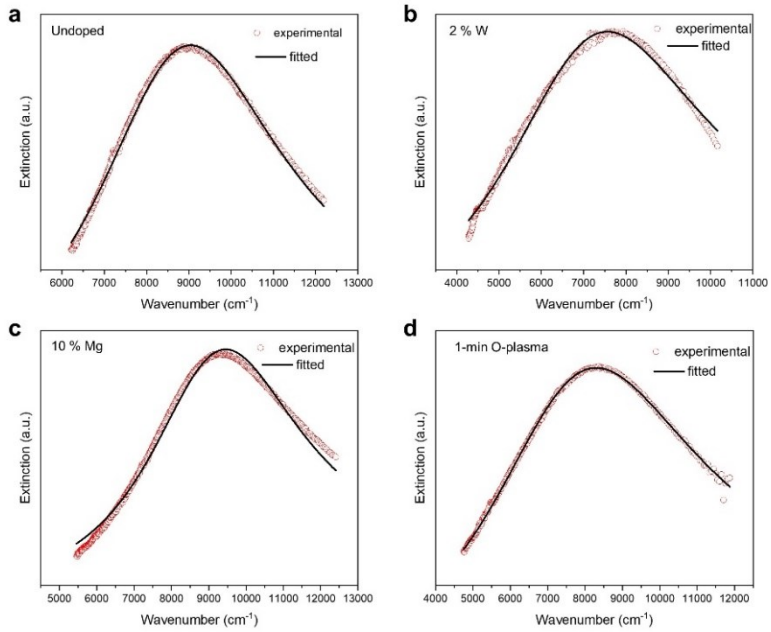

Fig. S9. Drude fitting of extinction peaks. Four samples are presented as examples for the Drude fitting of extinction spectra, including the a) undoped, b) 2% W-doped, and c) 10% Mg-doped VO_2 crystals as well as the d) undoped VO_2 after 1-min O-plasma treatment. Experimental and fitting data are indicated as red and black, respectively. The result shows a good alignment between the experimental and fitting data.

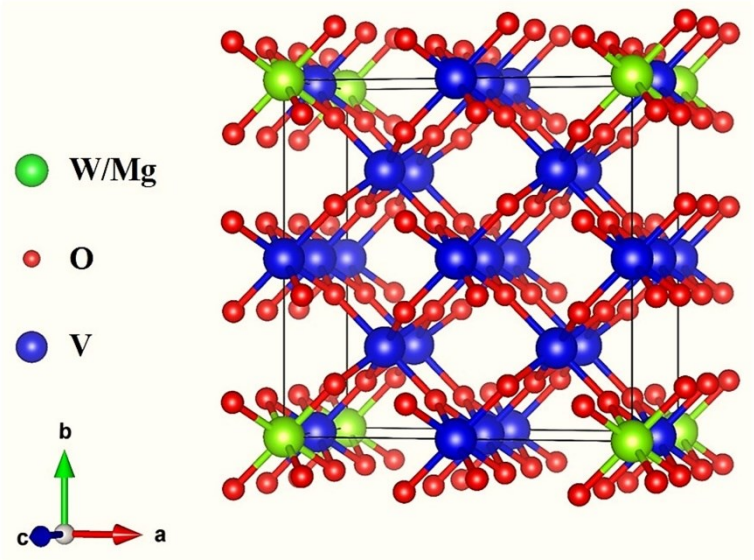

Fig. S10. The crystal structure for a 2*2*2 supercell containing 1 W/Mg atom and 15 V atoms, and hence the doping concentration is 6.25 at. % for W/Mg-doped VO_2. The crystal supercell of rutile phase is used in DFT simulation to understand W/Mg doping effects.

Supplementary Fig. 11-15

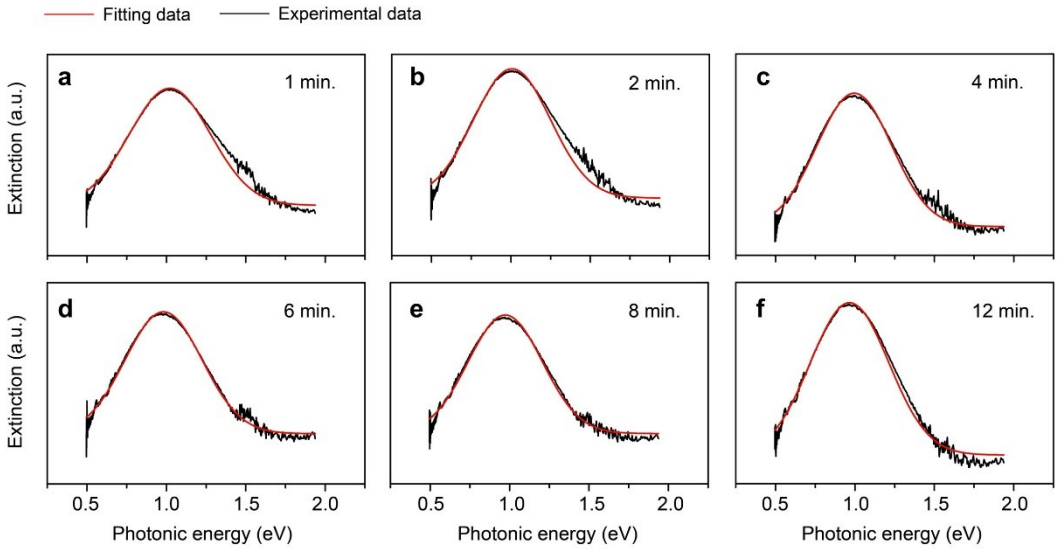

Fig. S11. Gaussian peaking fitting of plasma-treated samples. The LSPR FWHM is obtained by Gaussian fitting of the extinction peaks. The detailed Gaussian fitting results show as on the six samples with different O-plasma treatment duration from 1 to 12 min (Fig. S14a to f). The fitting and experimental data are indicated as the red and black lines, respectively. The two data are well-matched with each other on four samples.

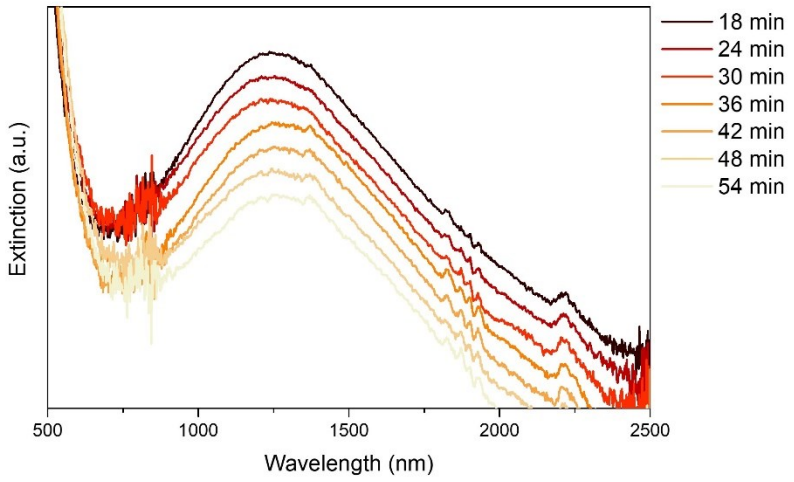

Fig. S12. The VO_2 sample under prolonging plasma treatment. The extinction spectra of pure VO_2 sample under prolonging O-plasma treatment that is more than 18 min. No obvious extinction peak shift is observed from 18 to 54 min.

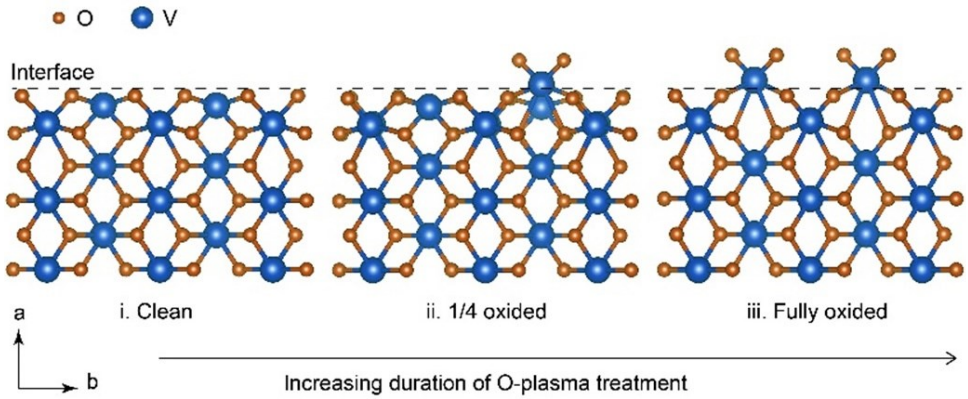

Fig. S13. The stable structure of VO_2 with clean, 1/4 oxidized and fully oxidized (0 0 1) surface was calculated via DFT methods. The oxidization degree increases under prolonging O-plasma duration.

It is observed two O adatoms bond with one exposed V atom, which forms a distorted octahedron with 6 bonded O atoms. The adsorbed O atoms force the bonded V atoms to stand out of the (0 0 1) surface plane.

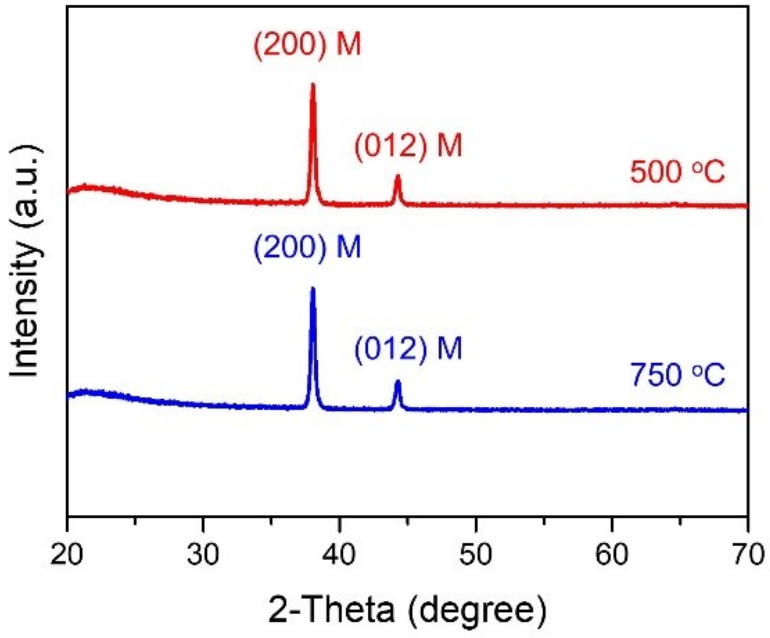

Fig. S14. Representative XRD results of the O-deficient VO_2 samples produced at the annealing temperatures of 500 and 750 °C. The monoclinic (200) and (012) phases are identified clearly on these samples, demonstrating the change of annealing temperatures in this range does not lead to the formation of any other impurity phases.

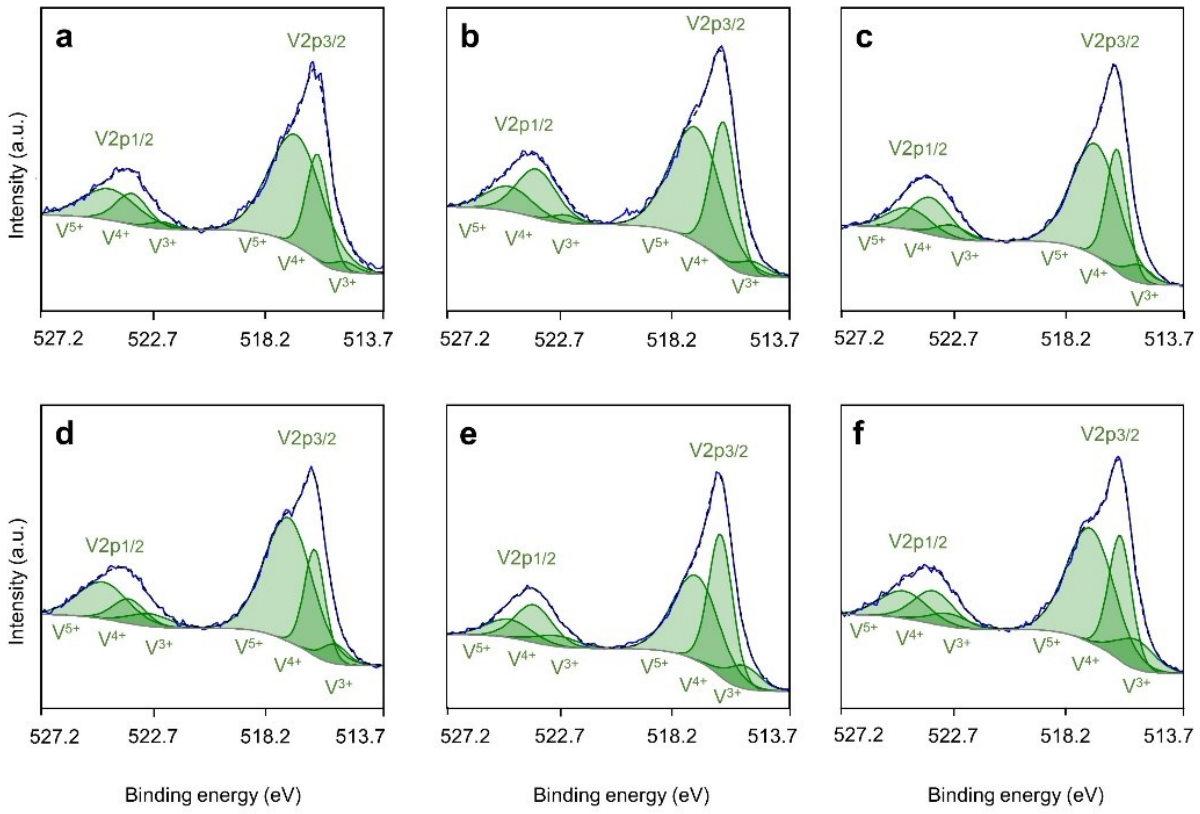

Fig. S15. a-f) XPS results and analysis of the O-deficient samples prepared under a gradient annealing temperatures of a) 500, b) 550, c) 600, d) 650, e) 700, and f) 750 ^{o}C.

Supplementary Fig. 16-20

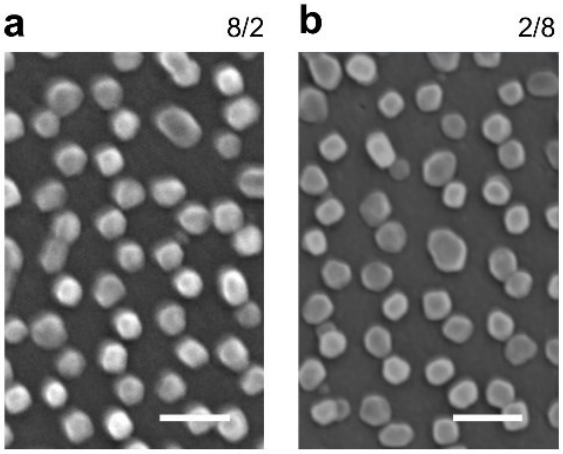

Fig. S16. Supplementary SEM images for co-doped samples. Representative SEM images of representative samples with W/Mg (%/%) doping levels of a) 8/2 and b) 2/8, respectively. All samples consist of hexagonal non-closed-packed NP arrays. Though defects exist, no obvious trend is observed under a series doping or co-doping level. The scale bars are 200 nm for the four images.

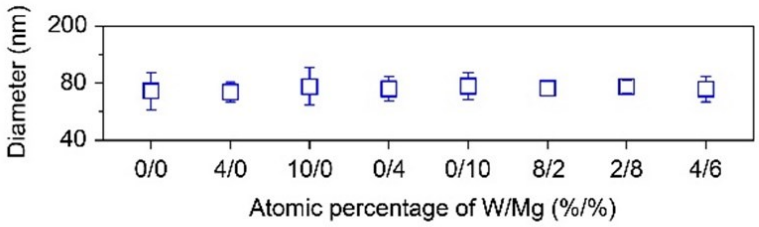

Fig. S17. Average diameter analysis of the produced samples with representative doping levels. The particle diameters are ~75–80 nm for all doping samples.

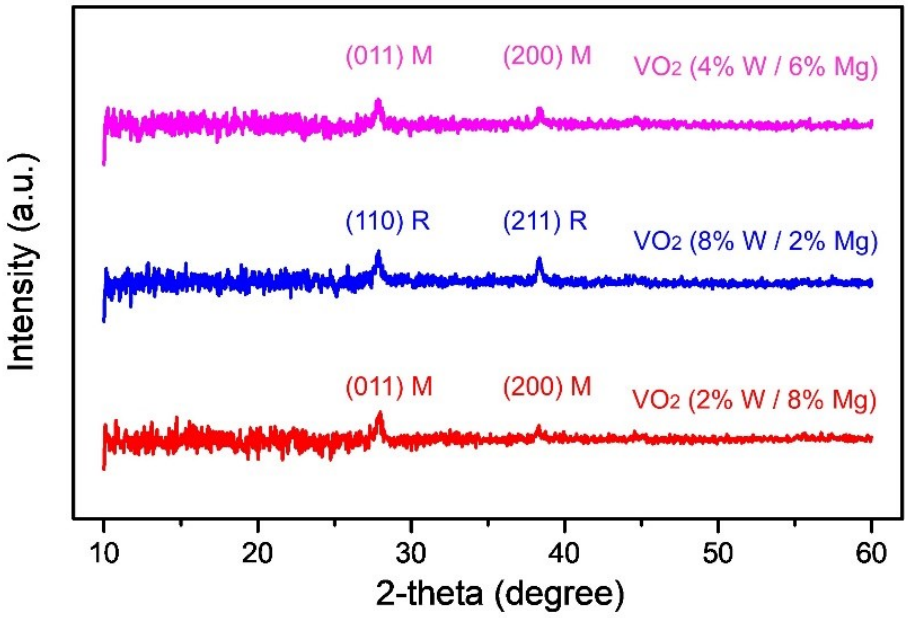

Fig. S18. Representative XRD results. The XRD measurement are conducted on four representative samples: the 4% W / 6% Mg (pink), the 8% W / 2% Mg (blue), and the 2% W / 8% Mg (red). All measurements are conducted at room temperature. The 8% W doping leads to a stable R phase at room temperature; thus the (110) R and (211) R crystal faces are identified on the 8% W / 2% Mg sample. As to the rest two samples, the crystal faces of (011) M and (200) M are identified. The result indicates the VO_2 (M/R) crystal structure maintains under such doping levels ($\leq$ 10%).

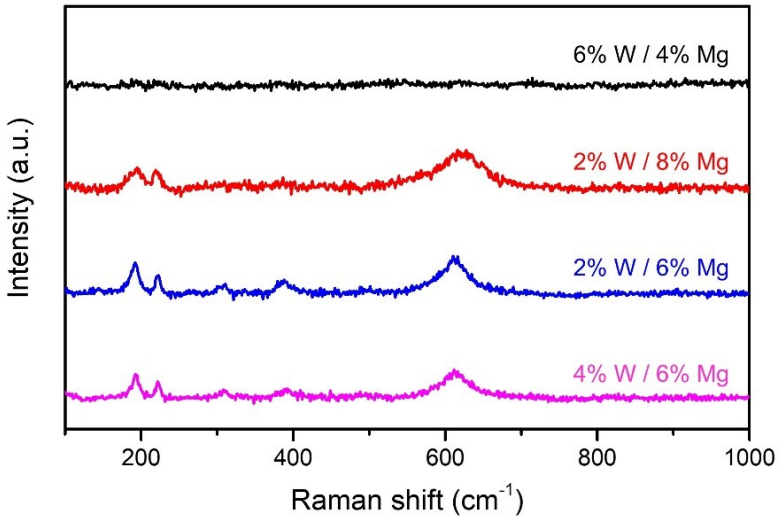

Fig. S19. Raman spectra of co-doped samples. The representative Raman spectra of four representative samples are recorded: the 6% W / 4% Mg (black), the 2% W / 8% Mg (red), the 2% W / 6% Mg (blue), and the 4% W / 6% Mg (pink) samples. Raman measurement of the four samples is conducted at room temperature. The 6 % W / 4% Mg sample shows the same spectrum as the high-temperature VO_2 (R) since the W-doping at such a level reduce the transition temperature and stabilized the R phase at room temperature. The rest three samples

display the same spectra as the VO_2 (M). The result indicates the VO_2 (M/R) crystal structure maintains under such doping levels (≤ 10%)

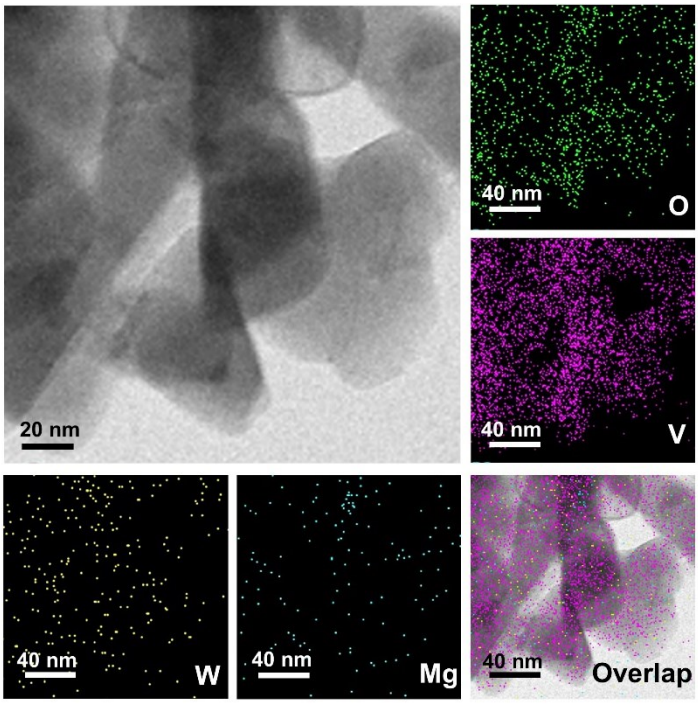

Fig. S20. TEM mapping. TEM image of the selected mapping area. The elemental maps of W, Mg, O, and V are indicated using different colours, and their overlap is also presented. The elements maps of W, Mg, O, and V overlap well with the TEM image of the NPs, indicating the successful introduction of the W and Mg dopants within the VO_2 NPs. It is observed that the elemental distribution is relatively homogenous and no obvious aggregation signals are observed on a crystal. The NPs are not in an array pattern due to the way it was prepared for TEM measurement. The crystals are scraped from quartz substrates and transferred to a TEM grid with the assist of ethanol.

Supplementary Fig. 21-26

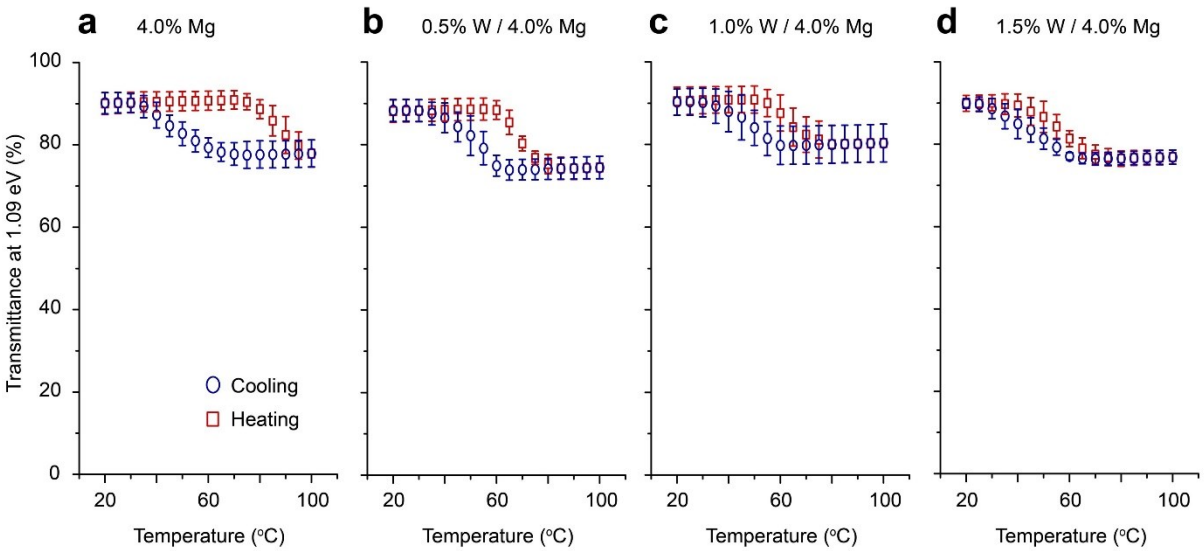

Fig. S21. Thermal hysteresis loops of the four individual layers. The thermal hysteresis loops are measured as the transmittance change at photonic energy of 1.09 eV. The hysteresis loops are recorded for the samples: a) the 4%-Mg, b) the 0.5%-W/4%-Mg, c) the 1.0%-W/4%-Mg, and d) the 1.5%-W\4%-Mg samples. Heating and cooling cycles are marked as blue and red, respectively.

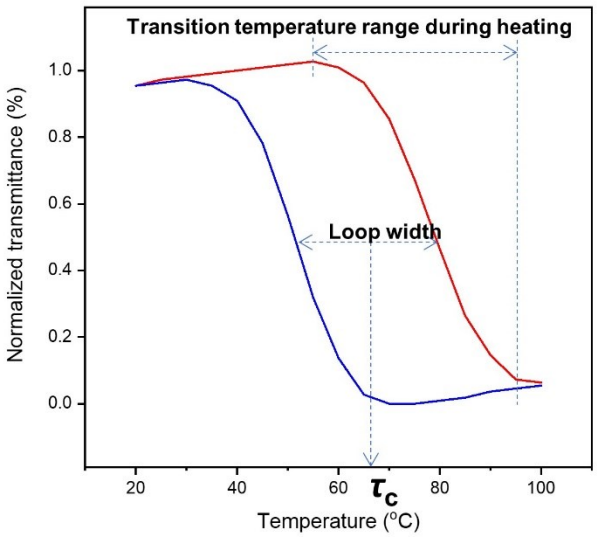

Fig. S22. The illustration of τ_c, loop width, and transition temperature range. The three parameters are illustrated in an example thermal loop of a typical VO_2 film. Normalized transmittance is applied. The heating and cooling processes are marked as red and blue, respectively.

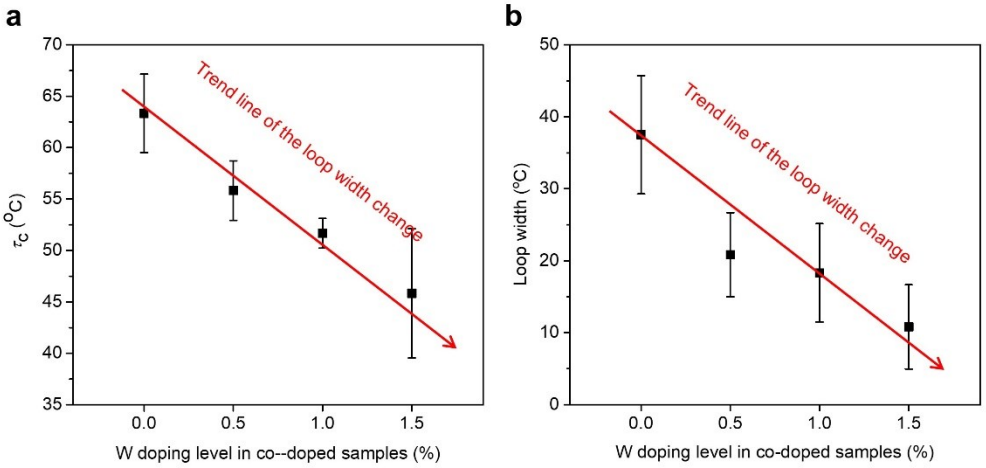

Fig. S23. Analysis of transition τ_c and loop width on co-doped samples. a) The measured τ_c on the Mg\W co-doped VO_2 NP samples with a different W-doping level. The τ_c is observed to decrease from ~63 °C at 0 at.% to ~46 °C at 1.5 at.%. The red line is the guidance for views to indicate the decreasing τ_c under an increasing W-doping level. Mg doping slightly decreases the τ_c since the 4% Mg-doped samples display a slightly low τ_c than 65-68 °C as in pristine VO_2. b) The effect of W doping level (at.%) on the loop width in the Mg\W co-doped VO_2 NP arrays. The loop width is observed to decrease under increase W doping level, indicated as the guidance for views (red line). For both the two analyses, the Mg doping level is fixed at 4 at.% and the W doping level varies from 0 at.% to 1.5 at.%.

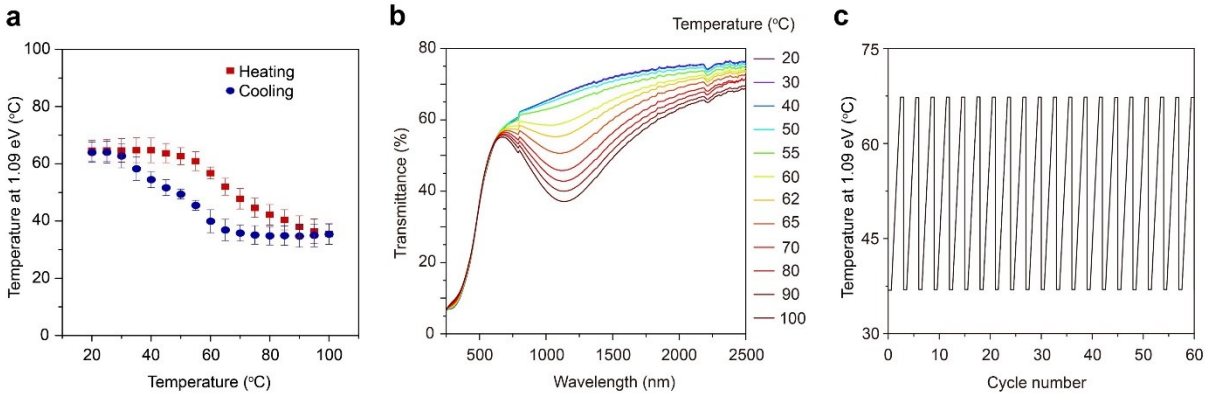

Fig. S24. Supplementary measurement of the multilayer sample. a) The transmittance hysteresis loops of the multilayer at photonic energy of 1.09 eV. The heating and cooling cycles are indicated as red and blue, respectively. b) The transmittance spectra of the multilayer sample under a cooling cycle from 100 to 20 °C. c) Stability test of the multilayer sample. The test is conducted by recording the transmittance change at 1.09 eV during heating-cooling procedures between 20 and 100 °C for up to 60 cycles. No obvious transmittance changes were observed during the 60 cycles.

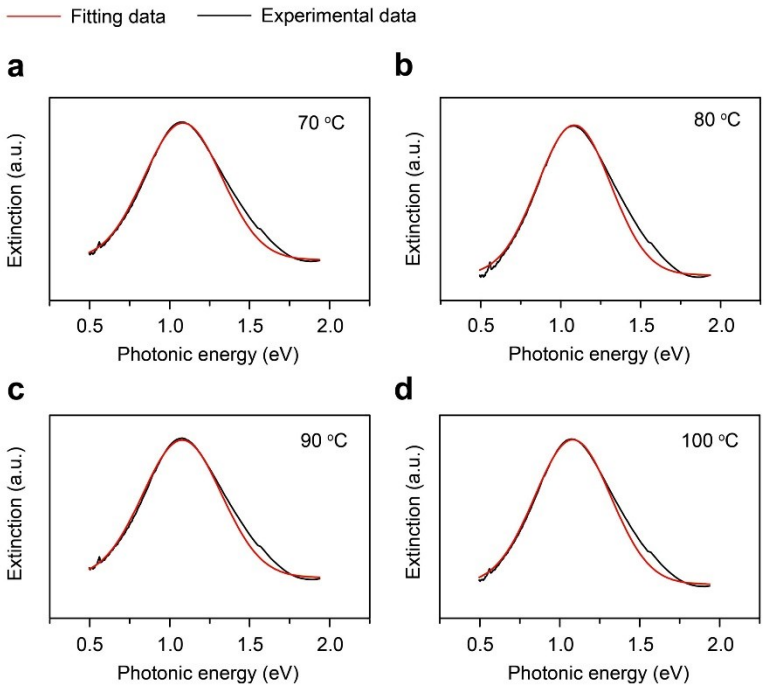

Fig. S25. Gaussian peaking fitting of the multilayer sample. The LSPR FWHM is obtained by Gaussian fitting of the extinction peaks. The detailed Gaussian fitting is presented as the multilayer sample measured under four representative temperatures: a) 70, b) 80, c) 90, and d) 100 °C. The fitting and experimental data are indicated as the red and black lines, respectively. The two data are well-matched with each other on four samples.

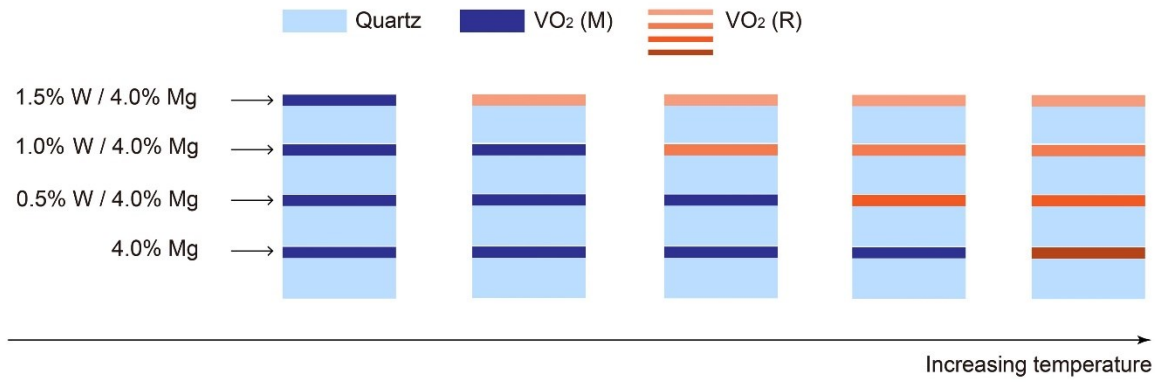

Fig. S26. Schematics of the transition in the multilayer sample. Under an increasing temperature, individual layers with a higher W-doping level transits to the R phase under lower temperatures. Thus, each layer transits to the R phase in sequence according to the W-doping level, and all samples reach the R phase under 100 °C. The VO_2 (M) and VO_2 (R) are indicated using different colours.

Supplementary Fig. 27-30

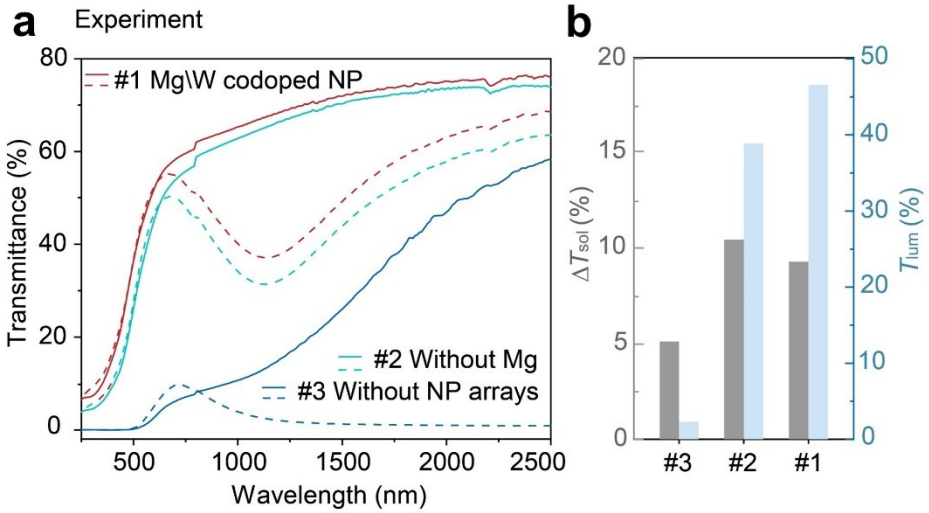

Fig. S27. The experiment result of LSPR-enhanced solar energy modulation. a) Transmittance spectra of multilayer samples with co-doped VO_2 NP arrays (#1), without the Mg-doping (#2), and without both the Mg-doping and the array structure (#3). b) Analysis of T_{lum} and ΔT_{sol} of the three samples in (a). The co-doped NP multilayer sample (#1) is compared with two reference samples (#2 and #3).

A transmittance valley at ~1150 nm is observed under high temperature on both sample #1 and #2 only, suggesting the NP array structure is essential for generating the NIR LSPR on VO_2 (R). Another advantage of NP array is its relatively low load of VO_2 compared to the planar film, leading to a higher transmittance. Both the sample #1 and #2 exhibit significantly promoted T_{lum} and ΔT_{sol}, compared to sample #3 without NP array structure. Moreover, sample #1 displays higher transmittance than sample #2, demonstrating the Mg dopants are efficient to increase the T_{lum}.

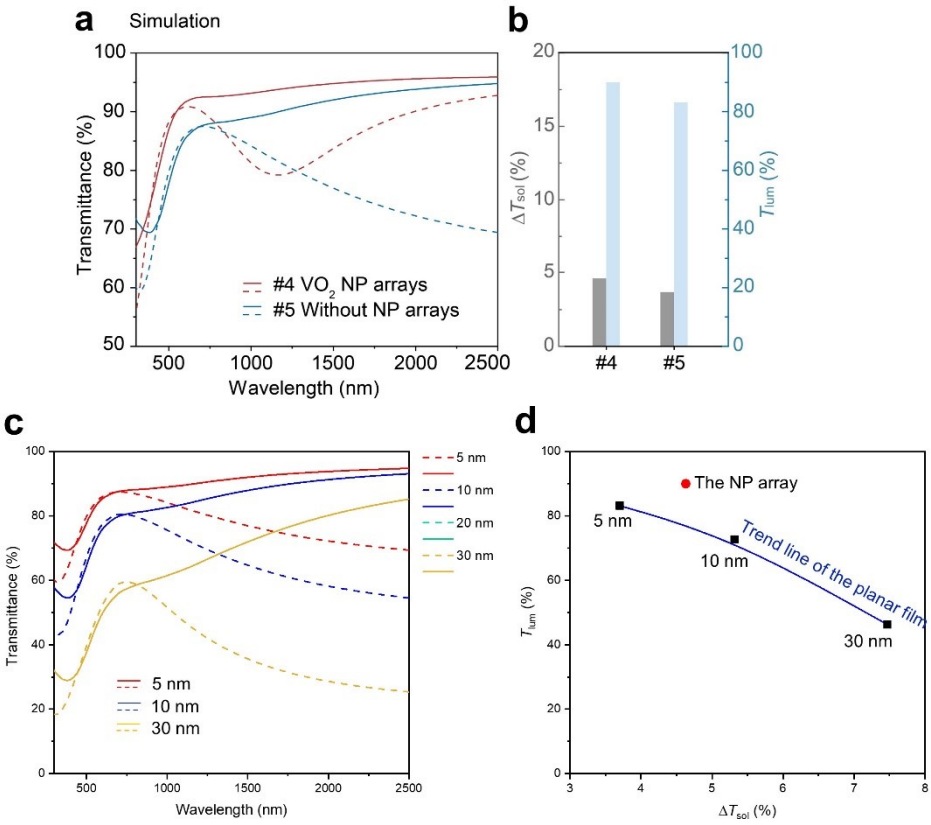

Fig. S28. Simulation result of LSPR-enhanced solar energy modulation. a) Simulated transmittance spectra of the film consisted of hexagonally patterned VO_2 NPs (#4) and a 5-nm planar VO_2 film (#5). b) Analysis of the T_{lum} and ΔT_{sol} of the two simulated sample in (a). c,d) FDTD calculation result of thin film VO_2. c) Simulated spectra of the planar VO_2 film with a thickness of 5, 10, and 30 nm under low (monoclinic VO_2, solid lines) and high temperature (rutile VO_2, dash lines). d) Performance analysis of the simulated planar VO_2 film (the black rectangles) and the comparison with the simulated NP array (the red dot). The blue line is the performance trend line of the planar films.

The simulation performs on a hexagonal VO_2 NPs array (#4) and planar VO_2 films with a thickness of 5 nm. The largest optical contrast is observed at 2500 nm on the 5-nm planar film and changes to the short wavelength with higher solar energy density on the NP sample. Comparing to 5-nm planar film (#5), the NP sample displays both a high T_{lum} (90%) and ΔT_{sol} (4.6%). Besides, the calculated NP sample outperforms the trend line of planar films with different thicknesses of 5-20 nm (Fig. S28 d).

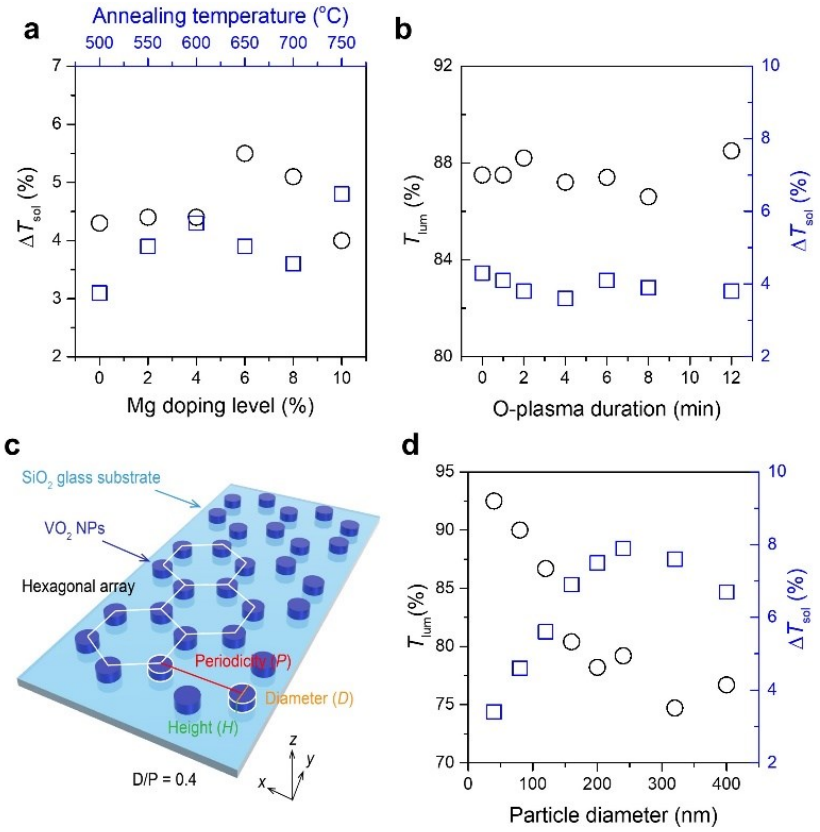

Fig. S29. a) Analysis of the ΔT_{sol} for samples with different Mg-doping levels and O vacancy (annealing temperatures). b) Analysis of the ΔT_{sol} and T_{lum} for the samples with controllable surface oxidization degrees, which controlled by the duration of O plasma post-treatment. c) E) Schematic of the model used in the FDTD method with characteristic parameters of periodicity (P), diameter (D), and height (H). The dielectric constant of pure VO_2 is applied and the D/P ratio is fixed to 0.4 and the H is fixed to 50 nm, which are close to the parameters in the experiment. d) Analysis of the ΔT_{sol} and T_{lum} of the simulated NPs with different D from 50 to 400 nm.

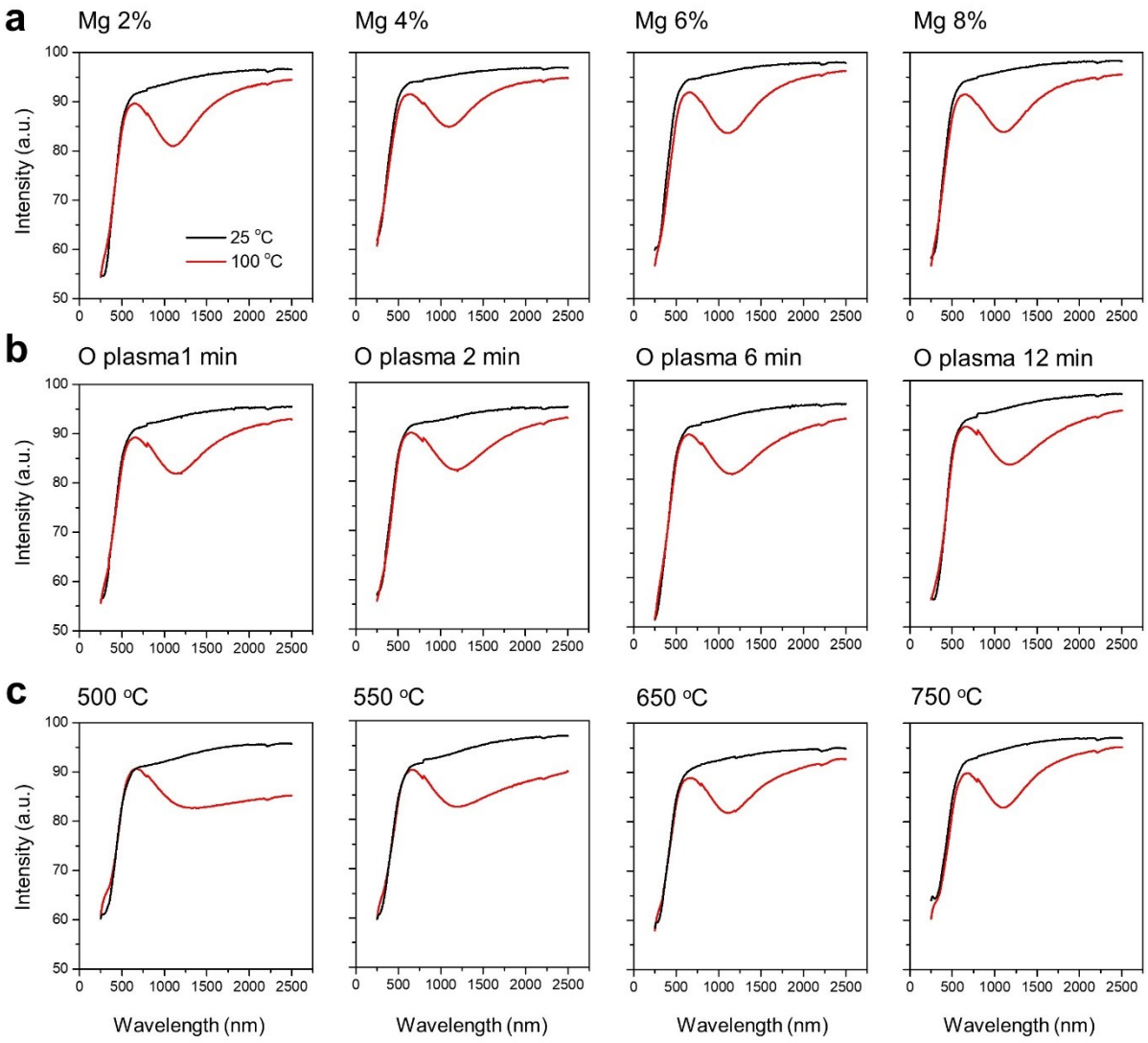

Fig. S30. a-c) Representative transmittance spectra of the atomic defective VO_2 samples were recorded at 25 °C and 100 °C for the low-temperature and high-temperature states, respectively. a) The transmittance spectra of Mg-doped samples with different doping levels. b) The spectra of surface-oxidized samples with controllable oxidization degrees using an O plasma post-treatment. c) The spectra of the O defective samples

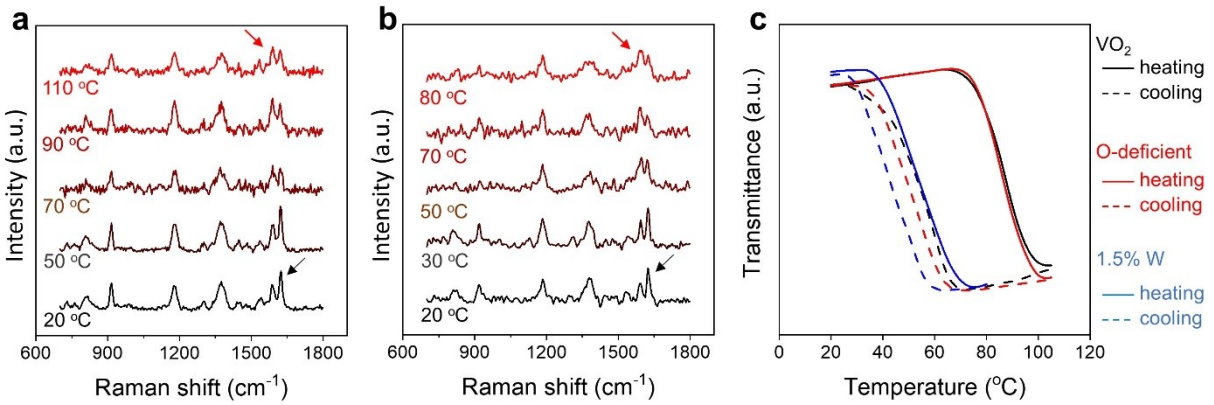

Fig. S31. a-b) Temperature-dependent Raman spectra of the crystal violet conducted using the substrates with a) the pristine VO_2 NP array and b) the 1.5% W-doped VO_2 NP array. c) Thermal hysteresis loops of the pristine, O-deficient, and 1.5% W-doped VO_2 samples. The 1.5% W-doped samples present a loop at lower temperatures than the pristine and O-deficient samples. The thermal hysteresis loops are measured as the transmittance changes at photonic energy of 1.09 eV.

Supplementary Table 1-4

Table S1 Drude fitting result of the W-doped VO_2

W doping level (at. %)	ω_p (cm^{-1})	Γ (cm^{-1})	N_e (10^{22} cm^{-3})
0.0	33834	5148.5	4.3
2.0	27838	5460.8	3.04
4.0	25984	5952.3	2.64
6.0	23445	5902.4	2.15
8.0	22799	5789.2	2.04
10.0	21622	5651.7	1.83

Table S2 Drude fitting result of the Mg-doped VO_2

Mg doping level (at. %)	ω_p (cm^{-1})	Γ (cm^{-1})	N_e (10^{22} cm^{-3})
2.0	33228	5192.5	4.32
4.0	34098	5004.8	4.55
6.0	34517	4975.1	4.67
8.0	34966	5031.4	4.79
10.0	35321	4921.3	4.89

Table S3 Drude fitting result of the plasma-treated VO_2

O-plasma duration (min)	ω_p (cm^{-1})	Γ(cm^{-1})	N_e (10^{22} cm^{-3})
1	31060	6978.4	3.78
2	30807	6652	3.72
4	29951	5855.4	3.5
6	29595	6397.8	3.43
8	29532	6079.3	3.42
12	29363	5713.5	3.38

Table S4 Drude fitting result of the O-deficient VO_2

Annealing temperature	ω_p (cm^{-1})	Γ(cm^{-1})	N_e (10^{22} cm^{-3})
500	25306	7472	2.50
550	30202	5336	3.57
600	33175	6461	4.3
650	33486	5302	3.41
700	34543	5015	4.69
750	34217	4994	4.59

Supplementary references

1. Y. Ke, X. Wen, D. Zhao, R. Che, Q. Xiong and Y. Long, *ACS Nano*, 2017, **11**, 7542-7551.
2. N. Wang, S. Liu, X. T. Zeng, S. Magdassi and Y. Long, *J. Mater. Chem. C*, 2015, **3**, 6771-6777.
3. Y. Ke, S. Ye, P. Hu, H. Jiang, S. Wang, B. Yang, J. Zhang and Y. Long, *Mater. Horiz.*, 2019, DOI: 10.1039/C9MH00065H.
4. Y. Ke, Y. Yin, Q. Zhang, Y. Tan, P. Hu, S. Wang, Y. Tang, Y. Zhou, X. Wen, S. Wu, T. J. White, J. Yin, J. Peng, Q. Xiong, D. Zhao and Y. Long, *Joule*, 2019, **3**, 858-871.
5. Z. Liu, Y. Zhong, I. Shafei, R. Borman, S. Jeong, J. Chen, Y. Losovyj, X. Gao, N. Li, Y. Du, E. Sarnello, T. Li, D. Su, W. Ma and X. Ye, *Nat. Commun.*, 2019, **10**, 1394.
6. W. H. Rosevear and W. Paul, *Physical Review B*, 1973, **7**, 2109-2111.
7. Y. Cui, Y. Ke, C. Liu, Z. Chen, N. Wang, L. Zhang, Y. Zhou, S. Wang, Y. Gao and Y. Long, *Joule*, 2018, **2**, 1707-1746.